

# Numerical Investigation of a Cavitating Model Propeller Including Compressible Shock Wave Dynamics

Bernd Budich<sup>1</sup>, Steffen J. Schmidt<sup>2</sup>, Nikolaus A. Adams<sup>3</sup>

<sup>1,2,3</sup> Institute of Aerodynamics and Fluid Mechanics, Technische Universität München  
D-85746 Garching, Germany

## ABSTRACT

A fully compressible numerical approach, combined with a homogeneous mixture model is applied to the simulation of the cavitating flow around the model propeller *VP1304*. The formally inviscid approach resolves the coupled behavior of phase transition and wave dynamics. It thus captures collapse-induced instantaneous pressure loads and associated shock wave dynamics and allows for an assessment of material erosion.

Our contribution focuses on a validation of the chosen approach with experimental and numerical investigations conducted in the frame of the *Potsdam Propeller Test Case 2011*. The obtained results show good agreement for the computed propeller efficiency, blade pressure distribution and observed cavitation pattern. A mesh alignment technique improves the accuracy of the propeller wake structure and enables the prediction of a cavitating trailing tip vortex. The investigations show that cavity dynamics cause instantaneous surface loads, originating from a periodic shedding of the suction side root cavity. Furthermore, stochastic collapse events lead to broad band noise. An investigation of the maximum pressure allows for a qualitative assessment of erosion risk.

## Keywords

Propeller Cavitation, Wave Dynamics, Cavitation Erosion

## 1 INTRODUCTION

Virtually all marine propulsion systems are affected by the occurrence of cavitating flow. Cavitation is not only a major source of noise and structural vibration due to the generated pressure fluctuations, it also leads to a degradation of propeller thrust and efficiency. Moreover, cavitation-induced erosion limits the lifespan of affected components (Carlton, 2012; Terwisga *et al.* 2007). Cavitation phenomena thus impose numerous limitations on ship propeller design. An in-depth understanding of the flow dynamics as well as predicting the expected material erosion is of particular interest.

Experimental analysis of ship propellers, however, is often complicated by accessibility constraints and available measurement techniques. Difficulties arise especially for detailed

investigations of internal flow features in cavitating regions. Furthermore, experiments within the controllable environments of towing tanks or cavitation tunnels are often preferred over full scale tests. Yet, difficulties arise concerning transferability from the model to the real-size product and repeatability of cavitation tests (Terwisga *et al.* 2007). Both aspects can only properly be assessed with expert knowledge about individual testing facilities. The situation is further complicated by the fact that direct observation of material erosion is not possible within the time frames available in the laboratory. Instead, as alternative to expensive long-term field tests at full scale, erosion risk can only be inferred from paint tests or the visual inspection of high-speed videos, refer e.g to Bark *et al.* (2014).

It is therefore advantageous to complement experimental work by numerical studies. The state-of-the-art are potential flow solvers, (U)RANS approaches or LES methods. Many computations are based on the incompressible description of the flow. With these methods, it is possible to properly predict propeller thrust and cavitation-induced break-down, capture cavitation patterns, as well as flow dynamics. In this respect, LES-based approaches, see e.g. Bensow *et al.* (2010), are the most promising for resolving delicate flow features.

In addition to the accurate prediction of propeller performance and flow dynamics it is desirable to derive quantitative criteria for material erosion risk and, possibly, erosion rates. From studies of single and multi-bubble arrangements it is well known that collapsing vapor structures create intense pressure peaks that lead to the formation of shock waves. Consequently, although the exact mechanism of material erosion is still unknown, an energy-cascade process is generally accepted in the literature, as summarized by Ziru (2012). The potential energy contained within macroscopic vapor structures is thereby converted into acoustic energy and focused towards the wall by a cascade of cavity implosions.

In order to accurately capture the collapse mechanism and collapse-induced pressure levels leading to erosive shock loads, it is essential to take the compressibility of the two-

phase flow into account. In the present work, we thus apply a fully compressible numerical method to simulate the cavitating flow around a model propeller geometry, with the aim to identify erosion-endangered areas.

This paper is structured as follows. In section 2, the selected test case is briefly presented. Section 3 subsequently discusses the applied method together with the underlying assumptions and shows the utilized computational setup. The results are then analyzed in section 4. Focus is first put on the validation with previous investigations of the same configuration by means of time-averaged quantities. Furthermore, the instantaneous flow is considered in more detail. The final part addresses the erosive impact on the propeller. Section 5 concludes with a summary of the findings and an outlook.

## 2 Test Case

For this study, the five-bladed, controllable-pitch model propeller *VPI304* is selected. It is characterized by a diameter of  $D = 0.25$  m and a chord length at  $r/R = 0.7$  of  $c_{0.7} = 0.104$  m. All investigations are carried out at the design pitch ratio  $P_{0.7}/D = 1.635$ , taken at  $r/R = 0.7$ .

The propeller has been investigated experimentally by the Schiffbau-Versuchsanstalt Potsdam (SVA Potsdam GmbH, 2011a,b,c). Furthermore, it was considered as the Potsdam Propeller Test Case (PPTC) at SMP'11 by 11 different groups<sup>1</sup>. The large database available enables a detailed validation of our approach.

In this investigation, we focus on the PPTC operating point 2.3.1, see SVA Potsdam GmbH (2011a), characterized by an advance coefficient  $J = V_a/nD = 1.019$ , computed with the advance velocity  $V_a = 6.37$  m/s and rate of revolution  $n = 24.987$  rev/s. The propeller is analyzed at both wetted as well as cavitating conditions. For the latter, a cavitation number of  $\sigma_n = (p_{\text{amb}} - p_{\text{vap}})/(1/2 \rho_{\text{ref}} (nD)^2) = 2.024$ , computed with the vapor pressure  $p_{\text{vap}}$  and the ambient pressure  $p_{\text{amb}}$ , is selected.

## 3 NUMERICAL APPROACH

### 3.1 Assumptions

For modeling phase transition, we apply a homogeneous mixture approach. Based on the assumption of local mechanical and thermodynamic equilibrium, the two-phase flow is treated as a single fluid. The pressure and velocities across phase boundaries are assumed to be continuous, i.e. surface tension and slip between the phases are neglected. Furthermore, temperature variations for a large body of water can be considered as small. An exception may arise during the last phase of concentric cavity collapses where high temperatures can be reached. However, the global behavior of the flow will

<sup>1</sup> For further reference on the Potsdam Propeller Test Case 2011, refer to the following individual publications of PPTC participants: Caldas *et al.* (2011), Fujiyama *et al.* (2011), Gaggero *et al.* (2011), Gatchell *et al.* (2011), Klasson *et al.* (2011), Li (2011), Liu *et al.* (2011), Morgut *et al.* (2011), Salvatore *et al.* (2011), Sipilä *et al.* (2011), and Yakubov *et al.* (2011).

not be altered. Therefore, we further assume barotropic flow and treat two-phase regions as isentropic, saturated mixture.

Due to the large disparity in momentum between liquid and vapor it can be reasoned that cavitating flow are predominantly inertia-driven. We thus choose to neglect viscosity, although an inclusion in the model is possible, which has been done recently by Egerer *et al.* (2014) and Örley *et al.* (2014).

Although these assumption are debatable for incipient cavitation, they apply to developed cavitating flows, such as the one investigated. On the other hand, as already motivated, compressibility can not be neglected in order to capture collapse-induced pressure peaks. As such, the flow is treated as fully compressible. The discussed approach can be utilized without any further assumptions or calibration parameters that are unknown *a priori*. Previous studies by Schmidt *et al.* (2011) show that a reliable prediction of collapse phenomena is possible, even in highly under-resolved cases where disperse mixtures are represented as a homogeneous fluid. Also complex flow configurations, where coexistence of various cavitation types and transition in between these forms occur, are captured (Schmidt *et al.* 2009; Schnerr *et al.* 2008). In addition, the method has been successfully applied by Mihatsch *et al.* (2012) for the assessment of erosion aggressiveness.

### 3.2 Method

Based on the assumptions summarized above, the governing equations for this study are the unsteady, compressible Euler equations. For a finite volume  $V$  with surface  $S$ , the equations within an inertial frame of reference read, in integral form:

$$\frac{\partial}{\partial t} \int_V \mathbf{q} dV + \int_S \sum_i n_i \cdot \mathbf{F}_i(\mathbf{q}) dS = \mathbf{0} \quad (1)$$

With  $\mathbf{F}_i(\mathbf{q})$  being the physical flux vector and  $\mathbf{q} = [\rho, \rho u, \rho v, \rho w]^T$  the vector of conserved quantities, namely the density  $\rho$  and the momentum flux  $\rho \mathbf{u}$ . The absolute velocity is denoted by  $\mathbf{u} = [u_x, u_y, u_z]^T$  and the outward-pointing normal vector on  $S$  by  $\mathbf{n} = [n_x, n_y, n_z]^T$ . Due to the assumption of barotropic thermodynamics, it is not necessary to solve the energy equation explicitly.

Rotation is handled by an Arbitrary-Eulerian-Lagrangian (ALE) approach, see e.g. Donea *et al.* (2004), which is applied to the complete computational domain. To this respect, the location of mesh vertices is updated explicitly each time step. Cell face velocities  $\mathbf{u}_{\text{mesh}}$  can be computed with the rotational velocity  $\boldsymbol{\omega}$  and the distance vector  $\mathbf{r}$  from the axis of rotation as  $\mathbf{u}_{\text{mesh}} = \boldsymbol{\omega} \times \mathbf{r}$ . The fluid convective velocity with respect to the grid evaluates to  $\hat{\mathbf{u}} = \mathbf{u} - \mathbf{u}_{\text{mesh}}$  and the physical flux vector in Eq. (1) is then defined as follows:

$$\mathbf{F}_i(\mathbf{q}) = \rho \hat{u}_i \begin{bmatrix} 1 \\ u_x \\ u_y \\ u_z \end{bmatrix} + p \begin{bmatrix} 0 \\ \delta_{1,i} \\ \delta_{2,i} \\ \delta_{3,i} \end{bmatrix} \quad (2)$$

Here,  $p$  denotes the pressure and  $\delta_{ij}$  the Kronecker delta.

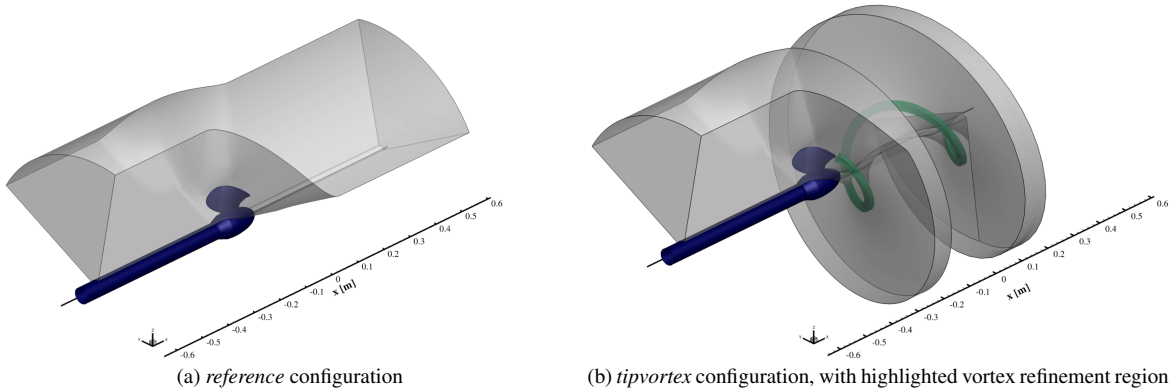


**Figure 1:** Computational domains utilized in this study.

The physical flux of Eq. (2) is approximated by a Godunov-type numerical flux function. Low-Mach-consistency ensures the correct asymptotic behavior for  $Ma \rightarrow 0$  (Schmidt *et al.* 2008). Spatial reconstruction of the face velocity utilizes the monotonic, non-linear limiter of Koren (1993), while an upwind reconstruction for the density and a 2<sup>nd</sup> order approximation for the interface pressure is applied.

Time integration is performed by an explicit 4-stage low-storage Runge-Kutta method. The time step is thus bounded by the CFL stability criterion and a CFL-number of  $CFL = 1.4$  is selected. Furthermore, time-operator preconditioning is employed during startup, as discussed in the next section.

Within the barotropic model, Eqs. (1)–(2) need to be closed by appropriate thermodynamic relations for the pressure  $p(\rho)$  and vapor volume fraction  $\alpha(\rho)$ . For the pure liquid ( $\alpha = 0$ ), a modified Tait-equation, see e.g. Sezal (2009), is used for obtaining the pressure. For water-vapor mixtures, the pressure is computed by integrating the equilibrium speed of sound  $c^2 = \frac{\partial p}{\partial \rho}|_s$ , taking the latent heat of vaporization into account, as described by Franc *et al.* (2004). The vapor volume fraction can then be expressed using the densities for the saturated liquid  $\rho_{l,sat}$  and vapor  $\rho_{v,sat}$  as  $\alpha = (\rho - \rho_{l,sat}) / (\rho_{v,sat} - \rho_{l,sat})$ . The saturation states of liquid and vapor are  $p_{sat} = 2339.3$  Pa,  $\rho_{l,sat} = 998.2$  kg/m<sup>3</sup> and  $\rho_{v,sat} = 0.0172$  kg/m<sup>3</sup>, evaluated at the constant reference temperature  $T = 20^\circ\text{C}$ .

The governing equations are spatially discretized using structured, body-fitted grids, distributed using a block-structured topology. Parallel domain partitioning and load balancing is achieved by employing the graph partitioner Metis (Karypis *et al.* 1998).

### 3.3 Computational Domain and Boundary Conditions

All simulations are carried out on a single  $72^\circ$  blade passage. The *reference* configuration of the computational domain is shown in Fig. 1a, with the  $x$ -axis as axis of rotation pointing downstream. The blade, mounted in push configuration, is located in the 12 o'clock position (along the  $z$ -axis).

For the body-fitted grid, an H-topology in conjunction with a butterfly mesh around the blade is applied. The inlet, outlet and radial boundaries are located in a distance of  $l = 2D$  from

the propeller. Sponge layers ensure that wave reflection from the interior of the domain is kept to a minimum. To reach the desired advance coefficient  $J$ , the axial velocity  $u_x$  is prescribed at the inlet. For the outlet, an asymptotic pressure boundary condition is employed, in order to obtain similarity in the cavitation number  $\sigma_n$ . At circumferential boundaries rotational periodicity is enforced, while radial boundaries and all material surfaces are modeled as slip-walls.

An accurate representation of the, possibly cavitating, trailing tip vortex necessitates a high spatial resolution. Without resolving the vortex accurately, numerical dissipation will result in a quick decay and capturing a cavitating core will be unsuccessful. Moreover, as the vortex location depends on  $J$ , this should be reflected in the meshing procedure. In contrast to unstructured meshes, however, structured grids pose severe restrictions on the shape and location of refinement regions. Refining regions of interest is often connected to an undesired increase in the number of cells in other areas as well, which unnecessarily raises the computational cost.

With the aim to improve the resolution of the tip vortex while keeping the refinement as localized as possible, a semi-automated method of aligning the structured mesh to the tip vortex has been developed. This method transforms the basic domain configuration within the propeller wake region into a helix by prescribing the pitch angle  $\Theta = \Theta(x)$ . A refined region within the H-topology, initially oriented axially, can thus precisely be aligned with the tip vortex.

The domain of the resulting *tipvortex* configuration after applying the alignment for *op-2.3.1* is displayed in Fig. 1b. In addition, the tip vortex refinement region within the propeller wake is also highlighted.

In preparation of the grid sequencing, described below, three different mesh resolutions, *coarse*, *medium* and *fine*, are created for both the *reference* and the *tipvortex* configuration.

**Table 1:** Properties of the utilized grid levels.

grid level	no. of cells	min. cell size	avg. timestep
<i>coarse</i>	$1.2 \cdot 10^5$	0.5 mm	$4.6 \cdot 10^{-8}$ s
<i>medium</i>	$6.6 \cdot 10^5$	0.2 mm	$2.2 \cdot 10^{-8}$ s
<i>fine</i>	$5.2 \cdot 10^6$	0.1 mm	$6.4 \cdot 10^{-9}$ s

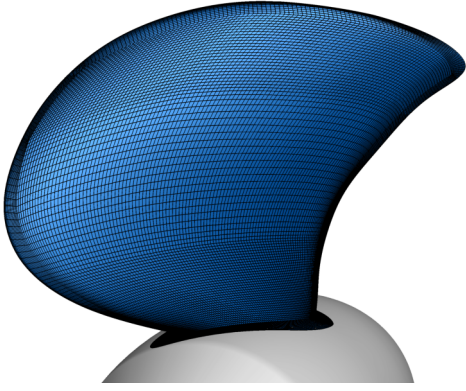


**Figure 2:** Visualization of surface mesh on the *fine* grid level.

The characteristics of the numerical grids utilized for this study are summarized in Tab. 1. The *fine* mesh consists of  $5.15 \cdot 10^6$  cells. The blade surface resolution for this grid, in terms of an average cell edge length in surface tangential and normal direction, is  $l_{\text{tan}} = 1$  mm and  $l_{\text{norm}} = 0.5$  mm, respectively. A visualization of the discretized blade surface on the *fine* mesh is given in Fig. 2.

## 4 RESULTS AND DISCUSSION

### 4.1 Simulation Startup

Due to the sudden start of the propeller, transient waves propagate within the domain during simulation startup. This process undesirably elongates the simulation time and in order to accelerate convergence, time-operator preconditioning (Turkel, 1999) is applied. By artificially lowering the speed of sound by a factor  $f_{\text{pre}}$ , the stiffness of the governing equations is reduced. The effect is two-fold: first, it allows to increase the CFL-bound time-step and second, acoustic waves are damped. Time-operator preconditioning yields convergence towards a steady state solution and is only employed for single-phase computations. No information concerning wave dynamics can be drawn. However, this is not required for the transient startup phase.

The problem statement of the PPTC requires to perform all computations at thrust identity under wetted conditions to gain better comparability for the propeller performance and the wake field behind the propeller. The advance coefficient  $J$  for the single-phase computation thus needs to be adjusted via the inflow velocity until the thrust coefficient  $K_T = T / \rho_{\text{ref}} n^2 D^4$  agrees with the measured wetted thrust coefficient  $K_T^{\text{ref}} = 0.387$ .

In this respect, a pre-conditioned simulation is conducted on the *fine* grid level in order to obtain the wetted thrust coefficient under the influence of pre-conditioning,  $K_{T,\text{pre}}$ . This is an estimate of the wetted  $K_T$  without utilizing pre-conditioning, because of the altered level of numerical dissipation. However, a sensitivity study regarding the influence of  $f_{\text{pre}}$  (omitted here for brevity) showed that the deviation is negligible when utilizing a value of  $f_{\text{pre}} = 10$ , while convergence is already sufficiently accelerated. The obtained  $K_{T,\text{pre}}$  can thus be utilized for adapting the advance coefficient  $J$  until the experimental value  $K_T^{\text{ref}}$  is reached.

Utilizing the adjusted inflow boundary condition, a grid sequencing procedure is applied: after obtaining an established, i.e. statistically converged, solution on one grid level, the flow field is interpolated to the next. The transient phase for the next refinement step can thereby be shortened significantly, reducing the computational cost.

### 4.2 Propeller Performance

For the present investigations, one iteration of the thrust identity procedure was sufficient in order to reach a wetted thrust coefficient of  $K_T = 0.389$  on the fine mesh, a deviation of less than 0.5% compared to the experiments. The advance coefficient  $J$  was increased by 6.5% with respect to the experiments. This rather large change is due to the fact that the inviscid method initially overestimates the propeller thrust. The approach is still pursued here in order to follow the methodology of the PPTC as close as possible.

Note that a more appropriate measure of these adjustments might be the angle of attack. It is changed by less than 2.3% (evaluated on the radius  $r/R = 0.7$ ) under the thrust identity adjustments.

The computed torque coefficient  $K_Q = Q / \rho_{\text{ref}} n^2 D^5 = 0.0965$  is slightly lower than the measurements, yielding a propeller efficiency of  $\eta_0 = J / 2\pi K_T / K_Q = 0.65$ , which is in good agreement to the reference value of  $\eta_0^{\text{ref}} = 0.63$ . The overestimation in propeller performance is to be expected due to fact that physical viscosity is neglected in the model.

To put these findings into context, Fig. 3 shows the propeller performance map. Here, the computed values of the non-dimensional thrust, torque and efficiency for the three grid levels are compared to the measurements by SVA Potsdam GmbH (2011a) and results from PPTC participants (see footnote 1 for a list of references). All values show very little deviation from the included references.

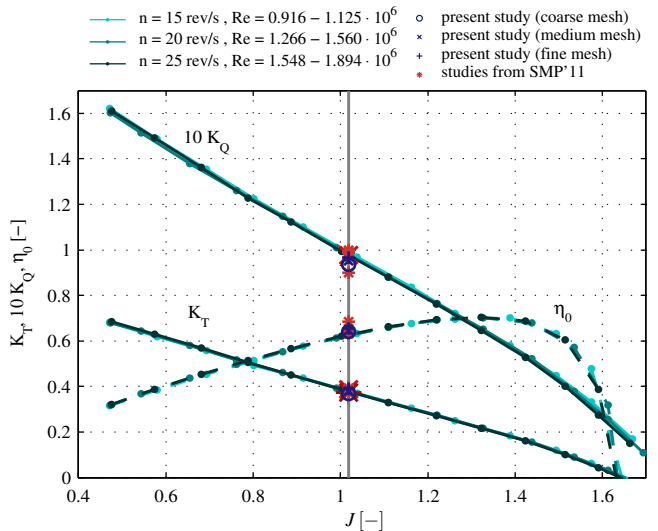


**Figure 3:** Propeller performance map, comparison between experimental reference (lines) and numerical investigations (symbols) of *VP1304* at operating point 2.3.1.

Since the propeller operates in the regime of thrust breakdown, the occurrence of cavitation results in a decrease in thrust, torque and efficiency. For the considered operating point, a thrust reduction by 3.5% is observed in the experiments. The computations equally show a reduction in thrust. However, with a time-averaged reduction by 7.5%, the break down is overestimated. This can be accredited to an enlarged cavity structure, as discussed in the following.

### 4.3 Averaged Flow Structure

**Cavity Extent** A validation of the computed cavitation structure is shown in Fig. 4. A sketch of the cavitation pattern observed experimentally is provided in Fig. 4a as a reference, while Figs. 4b and 4c show iso-surfaces of constant, time-averaged, vapor volume fraction  $\alpha$  for the fine mesh on the *reference* and *tipvortex* configuration, respectively. In contrast to sharp interface methods, single-fluid approaches raise the question which value of  $\alpha$  should be used for an equivalent representation. This aspect is not conclusively clarified in the literature. Therefore, Figs. 4b and 4c provide a visualization of  $\alpha = [0.1, 0.2, 0.5]$ .

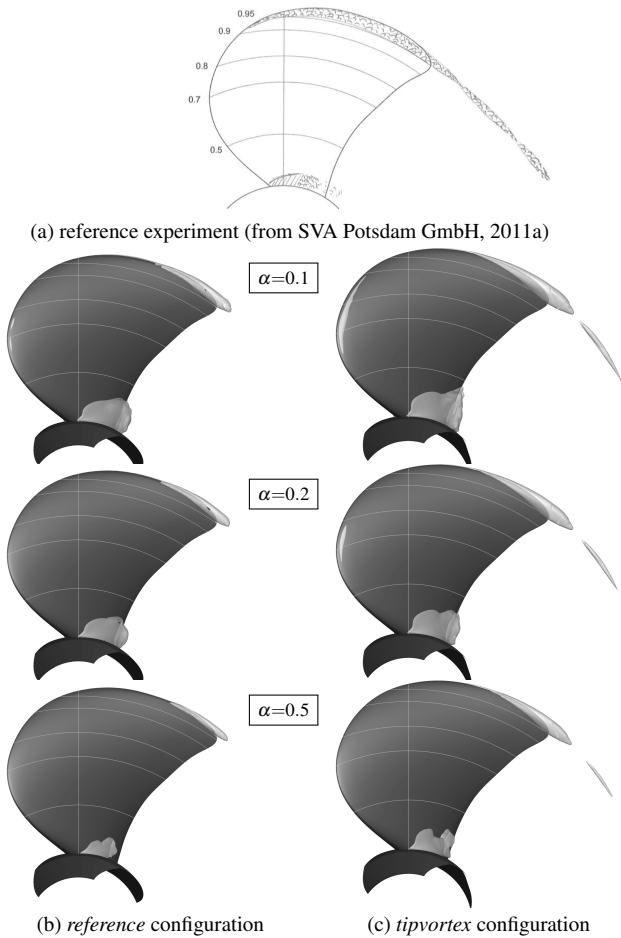


**Figure 4:** Cavitation pattern. Comparison between experimentally observed cavitation and present results in terms of time-averaged iso-surfaces of the vapor volume fraction  $\alpha$ .

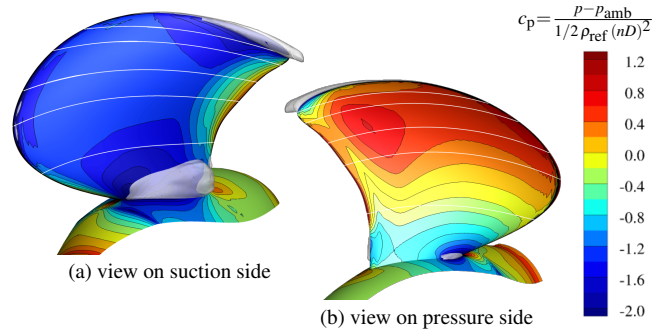


**Figure 5:** Time-averaged pressure coefficient  $c_p$  and iso-surface  $\alpha = 0.1$  (*reference* configuration, *fine* mesh).

A similar analysis was performed in the frame of the PPTC. It was concluded that participating numerical simulations show an overall tendency of overpredicting the extent of cavitation, while a void fraction of 50% yields the best agreement with the experiments. This conclusion also holds for the presented study. For this value of  $\alpha$ , the cavitation pattern obtained from the simulations agrees well in location and size with the references, especially regarding the extent of suction side root cavitation. Note that while leading edge cavitation was observed for most PPTC studies, it is almost absent from the present results. This can be attributed to some extent to the requirement of thrust identity corrections, changing the direction of relative flow towards the pressure side. However, the absence of leading edge cavitation is in agreement with the experiments.

Concerning the tip cavitation, inception is delayed towards the trailing edge. It can be assumed that the utilized wall-normal grid size of  $l_{\text{norm}} = 0.5$  mm is not sufficient near the leading edge to properly resolve tip vortex inception. However, the fundamental mechanism, stemming from the pressure gradient between pressure and suction side, is captured in the simulation and correctly predicts a cavitating vortex core in the rear part of the blade.

It can be assumed that the absence of physical viscosity in the model also influences the initial role-up of the vortex, which is situated within the boundary layer of the blade surface. However, it has to be acknowledged that the scaling behavior of the tip vortex is not fully understood yet (Terwisga *et al.* 2007). This can be accredited to some extent to the large differences in relevant Reynolds-numbers between model propellers and full scale experiments, which can amount to more than one order of magnitude. The operating point currently under investigation yields a relatively stable tip vortex. Therefore, it can be conjectured that the intended assessment of material erosion will not be affected.

Results from the *tipvortex* configuration show that increasing the resolution correctly promotes the formation of a cavitating trailing vortex, also within a time-averaged sense. Recondensation of the core occurs approximately at a position where the axial grid spacing increases, emphasizing that the mesh resolution plays a crucial role for capturing this feature.

**Blade Pressure Distribution** A visualization of the mean pressure coefficient  $c_p = (p - p_{\text{amb}})/(1/2 \rho_{\text{ref}}(nD)^2)$  is given in Fig. 5, together with an iso-surface of 10% vapor volume fraction. The suction side of propeller is characterized by a flat pressure distribution, Fig. 5a, while the pressure side, Fig. 5b, shows an increase in pressure with higher radius.

For the pressure distribution, no experimental references are available. However, a comparison with the other numerical investigations from the PPTC is possible as participants were requested to report on the section pressure coefficient  $c_{p,r} = (p - p_{\text{amb}})/(1/2 \rho_{\text{ref}} (V_a^2 + (2\pi nr)^2))$ .

This analysis is shown in Fig. 6 for the radii  $r/R = [0.7, 0.9, 0.95]$ . For wetted conditions, Fig. 6a, all simulations agree for large parts of the blade. Some discrepancies can be observed for the pressure side at  $r/R = 0.7$ . Here, the current simulation agrees with the majority of the references. Larger deviations, however, are present in the vicinity of the leading edge. The current study shows only a weak suction

side peak pressure, while most PPTC participants predict a strong negative pressure peak. Accordingly, under cavitating conditions, as shown in Fig. 6b, these computations also predict leading edge cavitation. This is not encountered in the experiments and the present simulation does not yield leading edge cavitation as well, as already discussed above.

**Propeller Wake** Detailed LDV measurements within the wake by SVA Potsdam GmbH (2011b) enable a further validation of the presented approach. Contrary to the above analyses, investigations are carried out at PPTC operating point *op-2.2*, characterized by  $J = 1.253$  and  $n = 23 \text{ s}^{-1}$ . Again, computations are conducted at thrust identity.

In Fig. 7, contour plots of the axial deficit velocity  $1 - u_x/V_a$  are shown on planes  $x/D = 0.1$  and  $x/D = 0.2$ , perpendicular to the axis of rotation. Results from the *reference* and *tipvortex* configuration, Figs. 7a and 7b, are compared with the measurements shown in Fig. 7c.

Regarding the structure of the wake, a good qualitative agree-

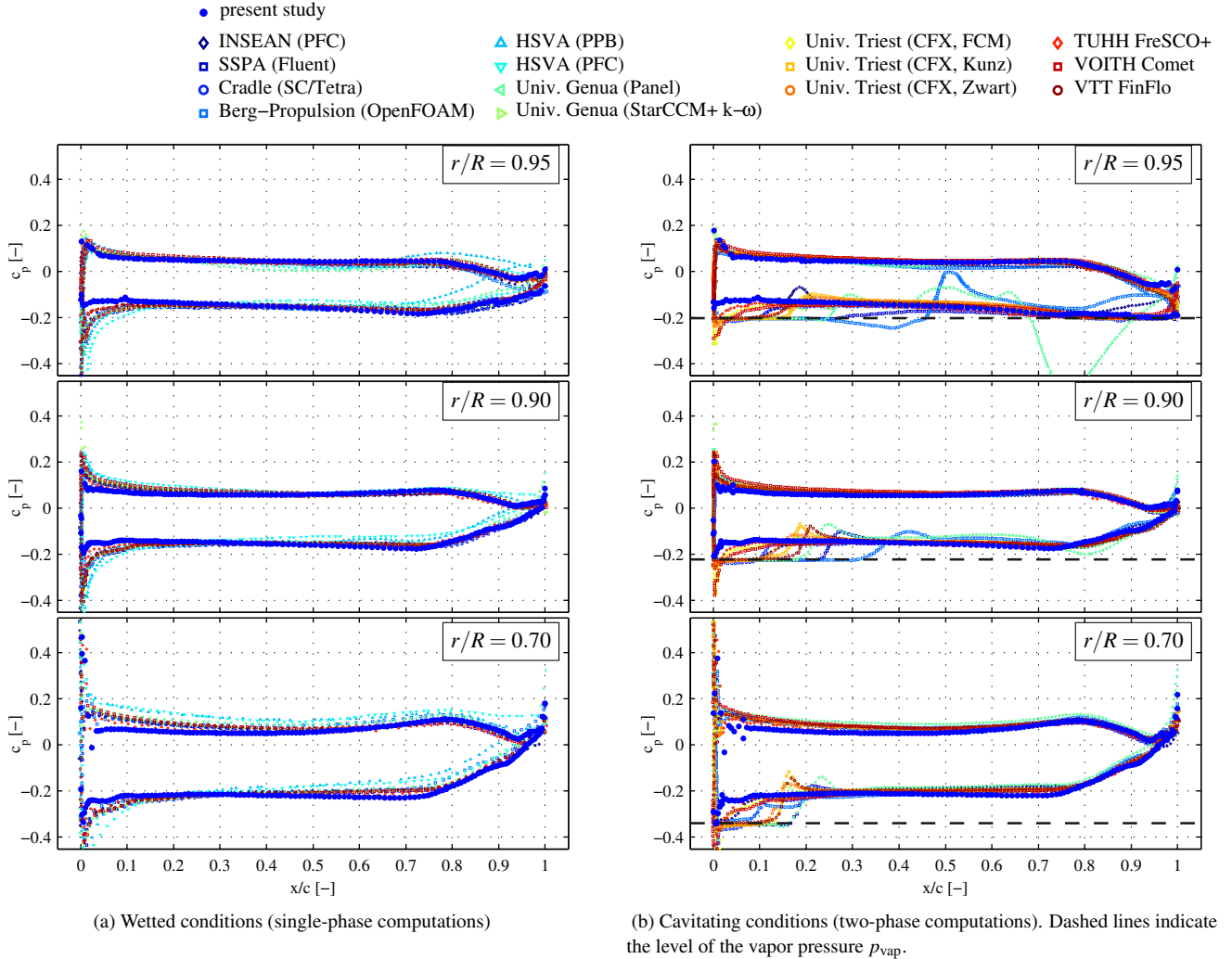


**Figure 6:** Non-dimensional section pressure coefficient  $c_{p,r} = (p - p_{\text{amb}})/(1/2 \rho_{\text{ref}} (V_a^2 + (2\pi nr)^2))$  on constant radii  $r/R = [0.7, 0.9, 0.95]$ . Comparison of the present results (*reference* configuration, *fine* mesh) and other numerical studies of the PPTC (see footnote 1 for a list of references).

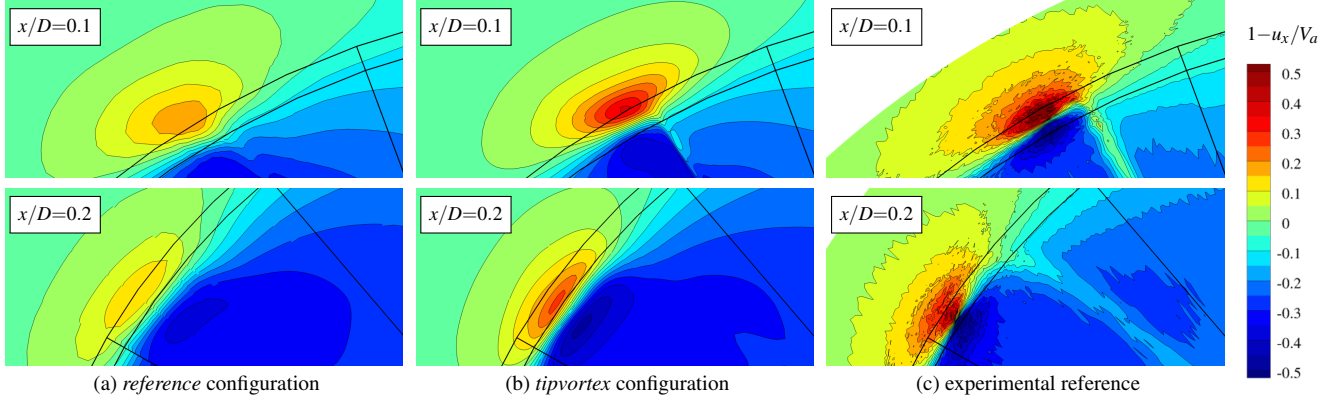


**Figure 7:** Contour plot of the deficit velocity  $1 - u_x/V_a$  on axial planes  $x/D = [0.1, 0.2]$ . Comparison between LDV measurements and present study (*reference* and *tipvortex* configuration, *fine* mesh). Radii  $r/R = 1.0$  and  $r/R = 0.97$  highlighted.

ment with the LDV measurements is observed. The visualization shows that the quality of prediction is significantly improved by the mesh alignment technique. The tip vortex structure on the *reference* mesh is noticeably smeared, while the agreement both in shape and strength is considerably improved for the *tipvortex* configuration.

A more detailed comparison of the obtained velocity field with the references is given in Fig. 8, showing the non-dimensionalized axial ( $u_x/V_a - 1$ ), radial ( $u_r/V_a$ ) and circumferential ( $u_\theta/V_a$ ) component on constant radii  $r/R = [0.95, 1.00]$  and axial positions  $x/D = [0.1, 0.2]$ .

The illustration shows that the wake structure is correctly reproduced by the simulations also for the individual velocity components. The deficit for the axial component is concentrated on a smaller region, which can be attributed to the absence of a boundary layer and the associated displace-

ment effect in the inviscid simulation. The agreement for the radial component, however, indicates that the strength of the tip vortex is correctly captured. Further downstream at  $x/D = 0.2$ , the overall lower mesh resolution leads to a dissipation of the tip vortex structure, but the agreement is still satisfactory.

#### 4.4 Instantaneous Flow Field

In the following, the instantaneous behavior of the cavitating flow is discussed in detail. The tip vortex remains relatively stable throughout the simulated time span, while the suction side root cavity is highly unsteady. It corresponds to a partial sheet cavity, repeatedly shedding vapor clouds.

This process is illustrated in Fig. 9. At the beginning of the shedding cycle, Fig. 9a, a new sheet is formed near the leading edge in the root section, with a vapor cloud from the previous cycle located further downstream. This vapor pattern is advected towards the trailing edge and the attached sheet grows in blade tangential direction, Fig. 9b. When the closure region of the cavity reaches the rear part, Fig. 9c, the adverse pressure gradient leads to the formation of a re-entrant jet. Directed upstream, it separates the sheet from the wall. As soon as the re-entrant jet reaches the front part of the partial cavity, Fig. 9d, the periodic process starts anew.

This cyclic behavior can also be illustrated by integral quantities, see Fig. 10. Here, the time evolution of the integral vapor content within the complete domain, Fig. 10a, as well as of the coefficients for thrust and torque, Fig. 10b, is displayed. Results are shown for the *coarse*, *medium* and *fine* mesh (*tipvortex* configuration), including the transient behavior when interpolating from one grid level to the next.

All quantities exhibit a highly unsteady behavior, stemming primarily from the shedding process discussed above. Note that a significant increase in the amount of integral vapor content is visible when transitioning to the *fine* mesh. This can be associated with the occurrence of cavitation in the core of trailing tip vortex within the propeller wake, which is not present on the coarser grid levels. Note also that the thrust

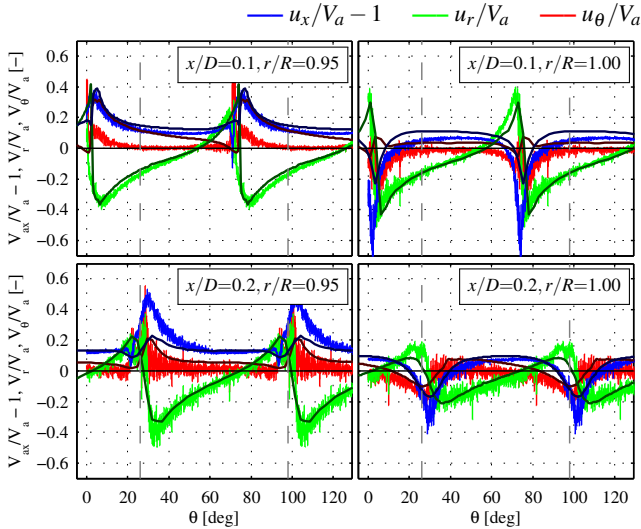


**Figure 8:** Axial, radial and circumferential velocity components on constant radii  $r/R = [0.95, 1.0]$  and axial positions  $x/D = [0.1, 0.2]$ . Comparison between LDV measurements (with indication of turbulence level as error bars) and present study (*tipvortex* configuration, *fine* mesh, solid line).

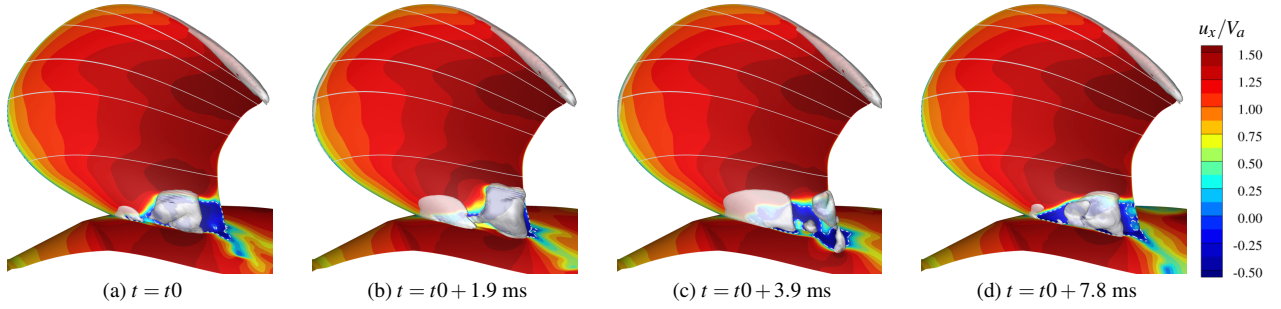


**Figure 9:** Time series of cloud shedding near suction side root. Contour plot of instantaneous axial velocity  $u_x/V_a$ , with contour-line  $u_x/V_a = 0$  to indicate progress of the re-entrant jet, and instantaneous iso-surface of  $\alpha = 0.1$ .

and torque coefficients are not noticeably influenced by this phenomenon. Beyond that, the thrust and torque coefficients show distinctive peaks superimposed on the global behavior associated with the shedding mechanism. These peaks are due to individual pressure pulses created by cavity collapse events near the blade surface.

More insight into the unsteady behavior can be obtained from a Fourier analysis. To this respect, a Fast Fourier Transformation (FFT) of the above quantities is applied in order to compute the corresponding Power Spectral Density (PSD). Transient portions of the signals associated with the grid sequencing are excluded from the analysis and a *Hanning* window is utilized in order to minimize edge effects.

This analysis is given in Fig. 11, showing the normalized, pre-multiplied power spectra  $f \cdot PSD$  of the integral vapor content, Fig. 11a, as well as thrust, Fig. 11b. Results for all three grid levels are included for completeness. However, simulation progress on the *fine* mesh is not sufficient yet in order to draw conclusions for this level. Thus, only results from the *coarse* and *medium* mesh are discussed in the following.

Two dominant frequencies,  $f_1 \approx 59.7$  Hz and  $f_2 \approx 137.6$  Hz, can be identified in both spectra. It thus can be concluded that cavity dynamics lead to an excitation of the material, that is close, but not equal, to the blade passing frequency (BPF). The spectra furthermore exhibit broad band noise at higher frequencies which is due to cavity collapse events and their stochastic behavior.

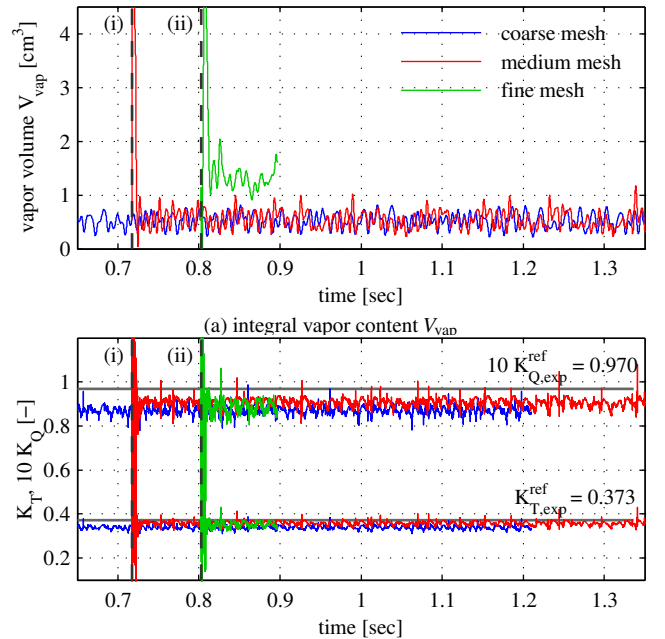
From visual inspection of the unsteady behavior, it is concluded that frequency  $f_2$  corresponds to the shedding mechanism of the suction side root cavity. With an average length of the attached sheet of  $l_{cav} = 32$  mm and a characteristic interface velocity of  $v_{cav} = V_a \sqrt{1 + \sigma_n} = 11.8$  m/s, the corresponding non-dimensional Strouhal-number can be evaluated as  $St = f_2 l_{cav} / v_{cav} \approx 0.37$ . This is in agreement with the commonly accepted range of 0.2 – 0.5 for shedding partial cavities (Dular *et al.* 2009).

The lower frequency  $f_1$ , present within both spectra, corresponds to a global pulsation of the cavitating structure as a whole. The reason is not finally clarified yet and further investigations in this direction are conducted.

#### 4.5 Erosion Risk Assessment

The presented simulation does not resolve events on a microscopic scale, such as the formation of micro-jets directed towards the wall or the collapse of micro cavities, because of an insufficient near-wall mesh resolution. It thus can only account for the collapse of macroscopic structures. Due to the inclusion of compressibility, the model captures these events and the associated, radiated shock waves. Through the assumption of an energy cascade eventually leading to material erosion, as discussed initially, it is reasonable to utilize these macroscopic events for an assessment of material erosion.

As discussed in the previous section, the suction side root cavitation exerts a shedding-like process, repeatedly leading to the creation of separated vapor clouds. Being advected into regions of higher pressure, these structures collapse and, consequently, create high pressure peaks. It was found that



(b) coefficients of thrust  $K_T$  and torque  $10K_Q$ , with indication of experimental reference under cavitating conditions

**Figure 10:** Time evolution of integral quantities, with indication of grid sequencing steps: (i) coarse–medium and (ii) medium–fine (*tipvortex* configuration).

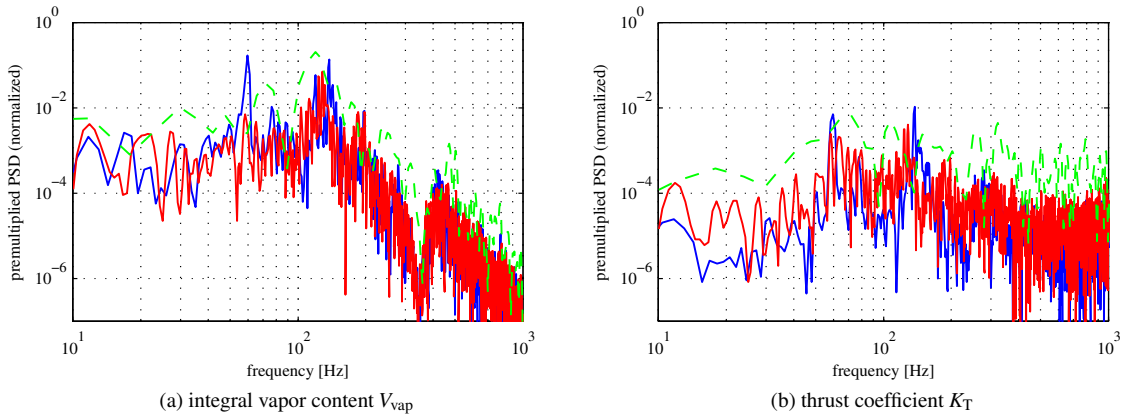


**Figure 11:** Fourier analysis of integral quantities (*tipvortex* configuration), legend identical to Fig. 10.

collapse events concentrate in the rear part of pressure recovery, with some variance due to the fragmentation of the vapor clouds into smaller structures after their detachment from the sheet cavity.

A time series for one of these events is shown exemplarily in Fig. 12. The instants selected in Figs. 12a – 12c show iso-surfaces of  $\alpha = 0.1$ , together with the static pressure as well as velocity vectors within the relative frame of reference on material surfaces. At  $t = t_0$ , Fig. 12a, a large vapor cloud has separated from the sheet. While the cloud is convected downstream, the sheet retracts under the influence of the re-entrant jet. In between these structures, a smaller, fragmented cavity is located. Due to the elevated pressure in the cavity closure region, collapse of this structure is initiated and it locally acts as a sink. Figure 12b shows the instant of cavity collapse. An intense pressure peak of  $p = 173$  bar is created, which is by a factor of  $> 400$  higher than the ambient pressure. This creates a shock wave that propagates into the liquid. As shown by Fig. 12c, the surrounding vapor structures lead to a distortion from its initially spherical shape. Also note that, due to the extremely short time scale of this event, the convective flow is not noticeably altered by the collapse event.

During the course of the simulation, the maximum pressure encountered within each cell is recorded. Collapses, like the one discussed above, consequently leave traces on the material. The collective impact pattern can thus be utilized to draw conclusions on erosion. A visualization of the maximum pressure on the surfaces after 2.5 revolutions of the propeller on the *fine* mesh is displayed in Fig. 13.

The visualization shows that elevated pressure levels are found in large parts of the suction side root area. A concentration of high-intensity collapses events can be identified in the rear part and directly on the trailing edge. Furthermore, the upstream area, corresponding to the location of the leading edge of the partial cavity sheet, exhibits higher pressures, although to a lesser extent. The origin is not fully understood at the moment and is currently under investigation. No traces of increased pressures are found near the blade tip, indicating that no erosion risk is predicted for the tip cavitation. The highest pressure of  $p_{\max} = 173$  bar stems from the collapse event discussed above.

In addition to these findings, the picture also illustrates that during the time span of 2.5 revolutions, corresponding to approximately 13 shedding cycles, only few strong collapse events occurred. Therefore, it can be reasoned that the covered time span is still too short. Simulations are currently continued in order to collect statistical data on longer time series.

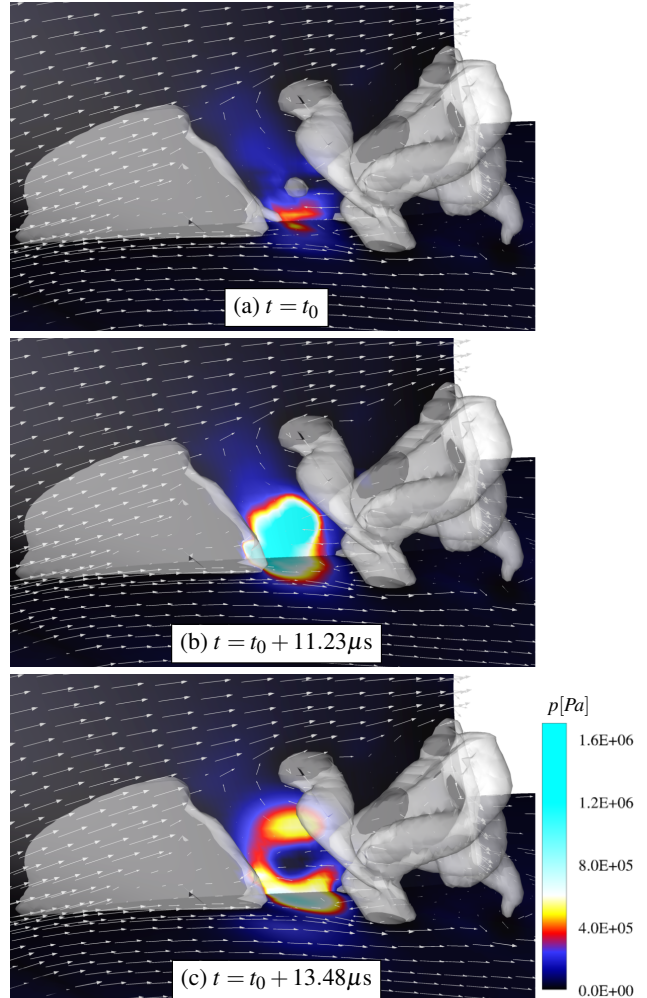


**Figure 12:** Time series of individual collapse event. Contour plot of instantaneous static pressure  $p$ , iso-surface  $\alpha = 0.1$  and relative velocity vectors on material surfaces.

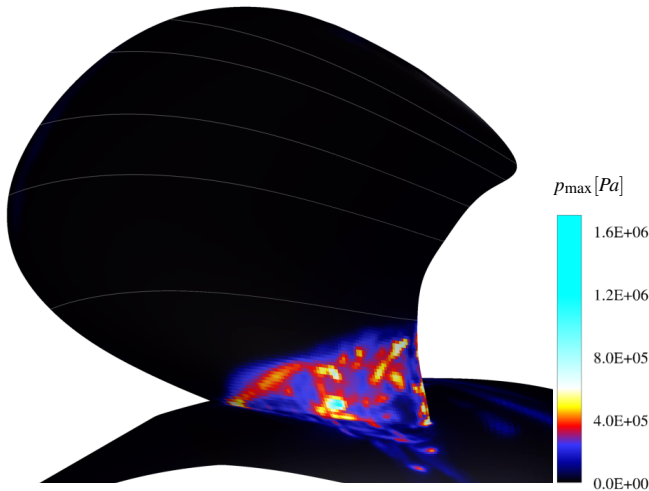


**Figure 13:** Maximum wall pressure after 2.5 revolutions of the propeller (*fine mesh, reference configuration*).

## 5 CONCLUSION

With the presented work, a fully compressible, density-based numerical approach, combined with a homogeneous mixture model is extended by an ALE approach in order to treat rotating configurations. Based on the assumptions of local equilibrium and barotropic thermodynamics, the developed method has been applied to the cavitating flow around a model propeller.

An important issue to consider is the large disparity of time scales between the convective flow and the wave dynamics, that need to be resolved by the compressible approach. Key aspects for the applicability of the chosen method are the grid sequencing procedure and time-operator preconditioning. In conjunction, both strategies proved to be successful in sufficiently shortening the initial transient phase. Thus, a developed flow field is quickly obtained, which subsequently can be evaluated, without pre-conditioning, including two-phase compressibility.

Physical viscosity is neglected in the numerical model. Therefore, the primary focus of this work is first put on a model validation. This is achieved by comparison with a large database available through the extensive experimental work by SVA and numerical studies in the framework of the Potsdam Propeller Test Case.

Demonstrated results show very good agreement with the references for the prediction of propeller thrust, torque and efficiency as well as for the blade pressure distribution. Although deviations can be found, they are comparable with other numerical investigations. These discrepancies can be accredited to some extent to the inviscid nature of the approach, but also to an insufficient spatial resolution. In this respect, the introduced mesh alignment technique for the structured grid proves to be advantageous. By significantly improving the accuracy of prediction for the velocity field within the propeller wake, it also reproduces the cavitating core of trailing tip vortex.

Furthermore, the overall pattern of cavitation matches well with the experimental reference, giving confidence that the chosen method can be utilized for the analysis of instantaneous flow features of the observed cavitation and an assessment of material erosion. First results have been presented, although longer statistics are needed. The analyses indicate that cavitation dynamics excite instantaneous pressure loads on the structure, stemming from the periodic shedding mechanism as well as from individual collapse events that lead to broad band noise. Moreover, first conclusions on erosion risk can be drawn through the maximum pressure criterion, suggesting that especially the rear part of the suction side root area as well as the trailing edge are prone to erosion.

In addition to the presented investigations, results from the *collapse detector*, developed by Mihatsch *et al.* (2012), are anticipated in order to analyze the erosive impact of the flow more quantitatively. By detecting distinctive collapse events in space and time, it allows to evaluate the flow aggressiveness on the basis of local collapse spectra. In addition, further grid refinements are envisioned in order to investigate the influence of the spatial resolution on the erosion prediction. Furthermore, investigations of the PPTC operating points 2.3.2 and 2.3.3 are currently conducted.

## ACKNOWLEDGMENTS

Support for this research was provided by the U.S. Office of Naval Research (ONR) and ONR Global through the NICOP entitled “Numerical Investigation of Ship-Propeller Cavitation with Full Description of Shock-Wave Dynamics” (Contract No. N62909-12-1-7034). The authors are grateful for Dr. Ki-Han Kim (ONR HQs) and Dr. Woei-Min Lin (ONR Global) for their support and guidance throughout this project. The authors further acknowledge the Gauss Centre for Supercomputing e.V. ([www.gauss-centre.eu](http://www.gauss-centre.eu)) for providing computing time on the GCS Supercomputer *SuperMUC* at the Leibniz Supercomputing Centre (LRZ, [www.lrz.de](http://www.lrz.de)).

## REFERENCES

- Bark, G. and Bensow, R. E. (2014). “Hydrodynamic Processes Controlling Cavitation Erosion”. *Advanced Experimental and Numerical Techniques for Cavitation Erosion Prediction*. Springer Netherlands, Dordrecht, 185–220.
- Bensow, R. E. and Bark, G. (2010). “Implicit LES Predictions of the Cavitating Flow on a Propeller”. *Journal of Fluids Engineering* 132 (4), 041302.
- Caldas, A., Meis, M., and Saraquete, A. (2011). “Open Water Test for Testing Methodology”. *Proc. of 2nd International Symposium on Marine Propulsors*. Hamburg, Germany.
- Carlton, J. S. (2012). *Marine Propellers and Propulsion*. Elsevier.
- Donea, J., Huerta, A., Ponthot, J., and Rodríguez-Ferran, A. (2004). “Arbitrary Lagrangian–Eulerian methods”. *Encyclopedia of Computational Mechanics*. Ed. by E. Stein, R. de Borst, and T. J. R. Hughes. John Wiley & Sons.

- Dular, M. and Bachert, R. (2009). "The Issue of Strouhal Number Definition in Cavitating Flow". Journal of Mechanical Engineering (55), 666–674.
- Egerer, C. P., Hickel, S., Schmidt, S. J., and Adams, N. A. (2014). "Large-eddy simulation of turbulent cavitating flow in a micro channel". Physics of Fluids 26 (8), 085102.
- Franc, J.-P. and Michel, J.-M. (2004). Fundamentals of Cavitation. Ed. by R. Moreau. Kluwer Academic Publishers.
- Fujiyama, K., Kim, C.-H., and Hitomi, D. (2011). "Performance and Cavitation Evaluation of Marine Propeller using Numerical Simulations". Proc. of 2nd International Symposium on Marine Propulsors. Hamburg, Germany.
- Gaggero, S., Villa, D., and Brizzolara, S. (2011). "SMP Workshop on Cavitation and Propeller Performances: The Experience of the University of Genova on the Potsdam Propeller Test Case". Proc. of 2nd International Symposium on Marine Propulsors. Hamburg, Germany.
- Gatchell, S., Hafermann, D., and Streckwall, H. (2011). "Open Water Test Propeller Performance and Cavitation Behaviour using PPB and FreSCO+". Proc. of 2nd International Symposium on Marine Propulsors. Hamburg, Germany.
- Karypis, G. and Kumar, V. (1998). "A Fast and High Quality Multilevel Scheme for Partitioning Irregular Graphs". SIAM Journal on Scientific Computing 20 (1), 359–392.
- Klasson, O. K. and Huuva, T. (2011). "Potsdam Propeller Test Case (PPTC)". Proc. of 2nd International Symposium on Marine Propulsors. Hamburg, Germany.
- Koren, B. (1993). "A robust upwind discretisation method for advection, diffusion and source terms." Numerical Methods for Advection-Diffusion Problems. Vieweg, 1–22.
- Li, D.-Q. (2011). "Prediction of Non-Cavitating and Cavitating Performance of a SVA Potsdam Propeller". Proc. of 2nd International Symposium on Marine Propulsors. Hamburg, Germany.
- Liu, D. and Hong, F. (2011). "The Numerical Predicted of SMP11 Propeller Performance with and without Cavitation". Proc. of 2nd International Symposium on Marine Propulsors. Hamburg, Germany.
- Mihatsch, M. S., Schmidt, S. J., Thalhamer, M., and Adams, N. A. (2012). "Quantitative Prediction of Erosion Aggressiveness through Numerical Simulation of 3-D Unsteady Cavitating Flows". Proc. of 8th International Symposium on Cavitation 2012. Singapore, 1–6.
- Morgut, M. and Nobile, E. (2011). "Numerical Predictions of the Cavitating and Non-Cavitating Flow around the Model Scale Propeller PPTC". Proc. of 2nd International Symposium on Marine Propulsors. Hamburg, Germany.
- Orley, F., Pasquariello, V., Hickel, S., and Adams, N. A. (2014). "Cut-element based immersed boundary method for moving geometries in compressible liquid flows with cavitation". Journal of Computational Physics, 1–57.
- Salvatore, F. and Greco, L. (2011). "Computational analysis of marine propeller performance and cavitation by using an inviscid-flow BEM model". Proc. of 2nd International Symposium on Marine Propulsors. Hamburg, Germany.
- Schmidt, S. J., Mihatsch, M. S., Thalhamer, M., and Adams, N. A. (2011). "Assessment of the Prediction Capability of a Thermodynamic Cavitation Model for the Collapse Characteristics of a Vapor-Bubble Cloud". Proc. of 3rd Warwick International Cavitation Forum. Warwick, England, 1–8.
- Schmidt, S. J., Sezal, I. H., Schnerr, G. H., and Thalhamer, M. (2008). "Riemann techniques for the simulation of compressible liquid flows with phase-transition at all Mach numbers-shock and wave dynamics in cavitating 3-D micro and macro systems". Proc. of 46th AIAA Aerospace Sciences Meeting and Exhibit. Reno, Nevada, USA.
- Schmidt, S. J., Thalhamer, M., and Schnerr, G. H. (2009). "Inertia controlled instability and small scale structures of sheet and cloud cavitation". Proc. of 7th International Symposium on Cavitation. Ann Arbor, Michigan, USA.
- Schnerr, G. H., Sezal, I. H., and Schmidt, S. J. (2008). "Numerical investigation of three-dimensional cloud cavitation with special emphasis on collapse induced shock dynamics". Physics of Fluids 20, 040703.
- Sezal, I. H. (2009). "Compressible Dynamics of Cavitating 3-D Multi-Phase Flows". PhD thesis.
- Sipilä, T., Siikonen, T., and Saisto, I. (2011). "FINFLO RANS-Predictions for Propeller Performance". Proc. of 2nd International Symposium on Marine Propulsors. Hamburg, Germany.
- SVA Potsdam GmbH (2011a). Potsdam Propeller Test Case (PPTC) - Cavitation Tests with the Model Propeller VP1304, Report 3753. Tech. rep.
- (2011b). Potsdam Propeller Test Case (PPTC) - LDV Velocity Measurements with the Model Propeller VP1304, Report 3754. Tech. rep.
- (2011c). Potsdam Propeller Test Case (PPTC) - Open Water Tests with the Model Propeller VP1304, Report 3752. Tech. rep.
- Terwisga, T. J. C. van, Wijngaarden, E. van, Bosschers, J., and Kuiper, G. (2007). "Achievements and challenges in cavitation research on ship propellers". International Shipbuilding Progress 54 (2-3).
- Turkel, E. (1999). "Preconditioning Techniques in Computational Fluid Dynamics". Annual Review of Fluid Mechanics 31 (1), 385–416.
- Yakubov, S., Cankurt, B., Maquil, T., Schiller, P., Abdel-Maksoud, M., and Rung, T. (2011). "Cavitation Simulations of the Potsdam Propeller Test Case". Proc. of 2nd International Symposium on Marine Propulsors. Hamburg, Germany.
- Ziru, L. (2012). "Assessment of Cavitation Erosion with a Multiphase Reynolds-Averaged Navier-Stokes Method". PhD thesis.

## DISCUSSION

### Question from Dmitriy Ponkratov

Are you planning to validate your erosive function against any model scale propeller, which showed erosion damage (paint removal)?

### Authors' Closure

Thank you for your question. Yes, a validation of both the maximum pressure criterion, as well as the collapse spectra provided by the collapse detector, is planned.

The methods utilized by our group for an assessment of flow aggressiveness and cavitation erosion prediction were recently validated by Mihatsch *et al.* (2015). The authors investigate a different configuration of a liquid expanding into a radially divergent gap, which exhibits unsteady sheet and cloud cavitation. For this configuration, good agreement between numerically predicted and experimentally measured impact load spectra, as well as a correlation between experimental pitting rates and collapse-event rates was obtained.

For the presently investigated case of cavitating ship propeller flow, a validation of predicted flow aggressiveness is also planned, preferably either through comparison with direct observation of erosion damage or by comparison with surrogate methods, such as paint removal tests on model scale propellers.

In this regard, we are currently searching for a suitable test case that could provide us with reliable data on actual or expected propeller erosion.

### Question from Tom van Terwisga

First I would like to express my appreciation for the results that you get out of your compressible Euler code. There is general acceptance that viscosity does not or hardly affect the sheet cavity extent and dynamics. But would you comment on the relevance of viscosity for tip vortex modelling and the blade root cavitation modelling? To my opinion, viscosity is likely to have a more pronounced effect here.

### Authors' Closure

Thank you for your question, which is much appreciated. There are configurations of caviating flow where viscosity has a dominant role, and thus can not be neglected. One example is the case of incipient cavitation. Similarly, it can be expected that viscosity is of importance for the development of the tip vortex, which forms due to the role-up of the viscous boundary layer. In order to properly capture the details of the role-up process, viscosity thus has to be taken into account. For the trailing portion of the tip vortex, viscosity plays a major role within the viscous core of the vortex. However, this effect is likely to be mitigated for a cavitating tip vortex. In this case, the presence of the vapor phase within the core region will be dominant and again reduce the influence of viscosity.

The topology of the blade root cavity, exhibiting an attached portion and subsequent shedding of vapor clouds, is closely related to the case of sheet cavitation. Therefore, it is assumed that the dynamics of this cavity are inertia-dominated.

Regarding the tip vortex, the above considerations will be relevant when the collapse-dynamics of the tip vortex will be of interest for an assessment of flow aggressiveness, e.g. due to inhomogeneous inflow situations. In the presently investigated configuration of homogeneous inflow, the stable tip vortex is expected to not cause any erosion on the propeller blade.

In order to better assess these aspects, we are currently conducting studies of the VP1304 propeller using compressible LES. However, it is to be expected that the consideration of viscosity in the model has only a subordinate role, given the grid resolutions that are currently affordable for the numerical investigation of cavitating ship propellers. At practically relevant Reynolds numbers, either a RANS approach, relying on a turbulence model, or under-resolved LES with wall-modelling can be employed. However, the role of these modelling approaches and the interference with cavitation as well as flow separation is still uncertain. Eventually, in order to fully capture the dynamics, e.g. of the cavitating tip vortex, LES with a much finer grid resolution, being fully resolved in the near-wall region of the blade and with a sufficient number of cells within the vortex core region, will be necessary.

## REFERENCES

- Mihatsch, M. S., Schmidt, S. J., and Adams, N. A. (2015). "Cavitation erosion prediction based on analysis of flow dynamics and impact load spectra". *Physics of Fluids* 27 (10), 103302.